

# New Constraints on the Supranuclear Equation of State and the Hubble Constant from Nuclear Physics – Multi-Messenger Astronomy

Tim Dietrich<sup>1,2</sup>, Michael W. Coughlin<sup>3</sup>, Peter T. H. Pang<sup>2,4</sup>, Mattia Bulla<sup>5</sup>, Jack Heinzel<sup>6,7</sup>, Lina Issa<sup>5,8</sup>, Ingo Tews<sup>9</sup>, and Sarah Antier<sup>10</sup>

<sup>1</sup> *Institut für Physik und Astronomie, Universität Potsdam,*

*Haus 28, Karl-Liebknecht-Str. 24/25, 14476, Potsdam, Germany*

<sup>2</sup> *Nikhef, Science Park 105, 1098 XG Amsterdam, The Netherlands*

<sup>3</sup> *School of Physics and Astronomy, University of Minnesota, Minneapolis, Minnesota 55455, USA*

<sup>4</sup> *Department of Physics, Utrecht University, Princetonplein 1, 3584 CC Utrecht, The Netherlands*

<sup>5</sup> *Nordita, KTH Royal Institute of Technology and Stockholm University,*

*Roslagstullsbacken 23, SE-106 91 Stockholm, Sweden*

<sup>6</sup> *Carleton College, Northfield, MN 55057, USA*

<sup>7</sup> *Artemis, Université Côte d'Azur, Observatoire Côte d'Azur,*

*CNRS, CS 34229, F-06304 Nice Cedex 4, France*

<sup>8</sup> *Université Paris-Saclay, ENS Paris-Saclay, Département de Physique, 91190, Gif-sur-Yvette, France*

<sup>9</sup> *Theoretical Division, Los Alamos National Laboratory, Los Alamos, NM 87545, USA and*

<sup>10</sup> *APC, UMR 7164, 10 rue Alice Domon et Léonie Duquet, 75205 Paris, France*

(Dated:)

The multi-messenger analysis of neutron-star mergers is not only of astrophysical interest, it also allows studying the behavior of supranuclear dense matter, probing the principles of general relativity, and measuring the expansion rate of the Universe. We perform a multi-messenger analysis of the gravitational-wave signal GW170817 and its electromagnetic counterparts AT2017gfo and GRB170817A, as well as the gravitational-wave signal GW190425. By incorporating information from the NICER observation of PSR J0030+0451, the radio observations of PSR J0740+6620, PSR J0348+4032, PSR J1614-2230, and nuclear-theory computations using chiral effective field theory, we provide new constraints on the neutron-star equation of state. Within our analysis, we determine the radius of a  $1.4M_{\odot}$  NS to be  $R_{1.4M_{\odot}} = 11.74^{+0.98}_{-0.79}$  km at 90% confidence and estimate the Hubble constant to be  $H_0 = 66.2^{+4.4}_{-4.2}$  km/Mpc/s at  $1\sigma$  uncertainty. The same multi-messenger-analysis techniques will be applicable for future observations, improving our understanding of the most extreme objects in the Universe.

*Introduction:* Recent progress in the field of multi-messenger astronomy allows us to address some of the most fundamental questions of current astrophysics research. In particular, the multi-messenger observation of binary neutron-star (BNS) mergers enables us to elucidate properties of matter under extreme conditions and to determine the expansion rate of the Universe. So far, the most prominent multi-messenger observation was the joined detection of gravitational waves (GWs), GW170817 [1], a gamma-ray burst (GRB), GRB170817A, a non-thermal GRB afterglow [2], and a thermal kilonova in the optical and near-optical bands, AT2017gfo [3], from the same astrophysical source. This event enabled already a new, independent measurement of the Hubble constant via GWs [4–6] and the observed kilonova [7, 8] and it allowed to place new constraints on the equation of state (EOS) of cold matter at supranuclear densities, e.g., [9–14]. While for the second GW observation of a BNS system, GW190425 [15], no electromagnetic (EM) counterpart was observed [16], the event increased the evidence that BNS systems will be regularly detected. Moreover, GW190425 and GW170817 have different properties and distances which shows the great diversity of BNS systems. Recently, also the dedicated observations of PSR J0030+0451 by the Neutron Star Interior Composition Explorer (NICER) [17, 18] improved our understanding of NS interiors and their surrounding

spacetime [19, 20].

In this article, we present a new nuclear physics – multi-messenger astronomy framework by combining knowledge from GW170817, GW190425, AT2017gfo, GRB170817A, PSR J0030+0451, PSR J0740+6620, PSR J0348+4032, and PSR J1614-2230 with nuclear-theory calculations of the EOS using chiral effective field theory (EFT) predictions at low densities. In contrast to previous studies, in which the GW analysis has been connected to nuclear-physics predictions, e.g., [9, 14], and to Bayesian analyses of EM and GW signals, e.g., [13, 21], or to studies combining GW and NICER results [22, 23], our study consistently combines all approaches: the GW signals GW170817 and GW190425, the kilonova signature of AT2017gfo, up-to-date constraints from nuclear-physics theory as well as radio and X-ray observations of pulsars, i.e., we are exploiting all possibilities that exist to date. In addition to new constraints on the supranuclear EOS, our method also provides an updated Hubble constant measurement. All analysis steps benefit from numerous advances with respect to previous works, among others: An updated waveform model [24] is employed to analyze the GW data GW170817 and GW190425, new and improved kilonova models are used to analyze AT2017gfo [25], and upgraded phenomenological relations that link the kilonova observation to source properties were derived from a large set of numerical-relativity

simulations where the new description overcomes inaccuracies of previous studies; cf. the discussion in [26].

*Multi-Messenger Analysis:* We use a multi-step procedure, as outlined in Fig. 1, to incorporate known constraints from nuclear theory and different astrophysical observations, i.e., we try to replace knowledge from a single-point-of-view analysis by combining different observables and information.

Our analysis starts from a large set of 5000 cold EOSs that describe the structure of NSs (upper left panel of Fig. 1). At low densities, these EOSs are constrained by microscopic calculations using chiral EFT interactions and advanced many-body methods. Chiral EFT is a systematic theory for nuclear forces that describes the interactions in terms of nucleon and pion degrees of freedom and includes all interaction mechanisms consistent with the symmetries of Quantum Chromodynamics [27]. The resulting forces are expanded in powers of momenta, resulting in an order-by-order expansion for nuclear interactions, which is then truncated at a given level. This systematic scheme allows us to estimate theoretical uncertainties from missing higher-order contributions to the nuclear interactions. The resulting nuclear Hamiltonian is then inserted into the Schrödinger equation which is solved using quantum Monte Carlo methods [28]. The radius of convergence of this expansion is limited to momenta below approximately 600 MeV [29]. Beyond this so-called breakdown scale, chiral EFT interactions and their uncertainty estimates are not reliable anymore. While recent analyses suggest that chiral EFT might be valid up to twice the nuclear saturation density [23, 30],  $n_{\text{sat}} = 0.16 \text{ fm}^{-3}$ , we adopt a more conservative limit and constrain our EOSs with chiral EFT calculations up to densities of  $1.5 n_{\text{sat}}$ . At densities above  $1.5 n_{\text{sat}}$ , we employ a model-agnostic parametric expansion scheme that represents the EOS in the speed of sound plane [31] and respects causality. The resulting EOS set is shown in the top row of Fig. 1.

In the next step, we restrict our set of EOSs by enforcing a maximum NS mass with an upper bound of  $M_{\text{max}}^{\text{sup}} = 2.16^{+0.17}_{-0.15} M_{\odot}$ , where the errors denote the  $2\sigma$  uncertainty [32]. This upper bound is derived from the consideration that the final merger remnant of GW170817 was a black hole. A lower bound of the maximum mass can be derived by combining radio observations of PSR J0740+6620 [33], PSR J0348+4042 [34], and PSR J1614-2230 [35]. We show the final posterior for the maximum mass in the top middle panel of Fig. 1 for better illustration. Based on the probability density function for the maximum NS mass, we can already discard some of the precomputed chiral EFT EOSs, and highlight favored EOSs (Fig. 1).

In the third step, we include the NICER results using the full posterior of the probability density function of Ref. [17]. Our analysis is based on the three-oval-spot pulse waveform model (blue shaded region). Comparing with other pulse models [17, 18] one finds general agreement between all predictions, so that so that systematic

uncertainties seem to be under control. The final ‘restricted’ set of EOSs is shown in the top right panel of Fig. 1, where each particular EOS has a given probability according to the maximum NS mass and NICER constraints. The EOSs, together with their given probabilities, are the input for our multi-messenger interpretation of GW170817 and AT2017gfo.

By sampling over the obtained EOS set under consideration of their precomputed weights, we analyze the GW event GW170817. In general, NS properties are inferred from GW signals due to the measurement of tidal effects, which are larger for NSs with smaller masses and larger radii. We employ the parallel `bilby` framework [36] and the new waveform model `IMRPhenomPv2_NRTidalv2` [24] for cross-correlation with the observed data and to infer the binary properties from the measured signal. This model is an upgrade of the waveform approximant `IMRPhenomPv2_NRTidal` which has been used as the state-of-the-art tool in the analyses of GW170817 [37] and GW190425 [15].

In the next step, we analyze the EOS with respect to AT2017gfo. Our EM analysis is based on an improved lightcurve model [25]. To draw conclusions about generic sources, we use a Gaussian-Process-Regression framework to compute generic lightcurves for various ejecta-mass properties. To connect the individual ejecta parameters to the properties of the system, we assume that the total ejecta mass, inferred from the analysis of the lightcurves, is a sum of multiple components: dynamical ejecta  $M_{\text{ej}}^{\text{dyn}}$  and disk-wind ejecta  $\zeta M_{\text{disk}}$ :  $m_{\text{ej}} = M_{\text{ej}}^{\text{dyn}} + \zeta M_{\text{disk}} + \alpha$ . The parameters  $\alpha$ , corresponding to a potentially unmodelled ejecta component, and  $\zeta$ , determining how much mass of the disk is ejected, are unknown and used as free parameters during our analysis. While our interpretation of the dynamical ejecta is based on previous work [21], we employ a new model for the disk-wind ejecta. This improved model is motivated by recent results outlining shortcomings of previous studies for systems with high mass ratios [26]. To overcome this issue, we include explicitly a mass-ratio dependence in the disk-mass prediction. To make use of the multi-messenger nature of our analysis, we use the GW results as an input for the analysis of AT2017gfo, i.e., the chirp mass, the mass ratio, and the EOS determine the prior for our EM study. Following this procedure, we further constrain the EOS models. To better quantify our results and enable easy comparisons with other works, we have calculated the radius of a typical  $1.4 M_{\odot}$  NS at 90% confidence. We quote the extracted radii at each stage in our analysis in Fig. 1. Including all parts of the analysis so far, we obtain the radius of a  $1.4 M_{\odot}$  NS of  $R_{1.4 M_{\odot}} = 11.67^{+0.92}_{-0.80} \text{ km}$  at 90% confidence.

These multi-messenger results can be used as further input for the analysis of the second observed BNS merger, GW190425. Due to the high total mass of GW190425, which generally suppresses tidal effects, we find that the inclusion of GW190425 does not lead to a noticeable improvement. Hence, our final estimate on the radius of

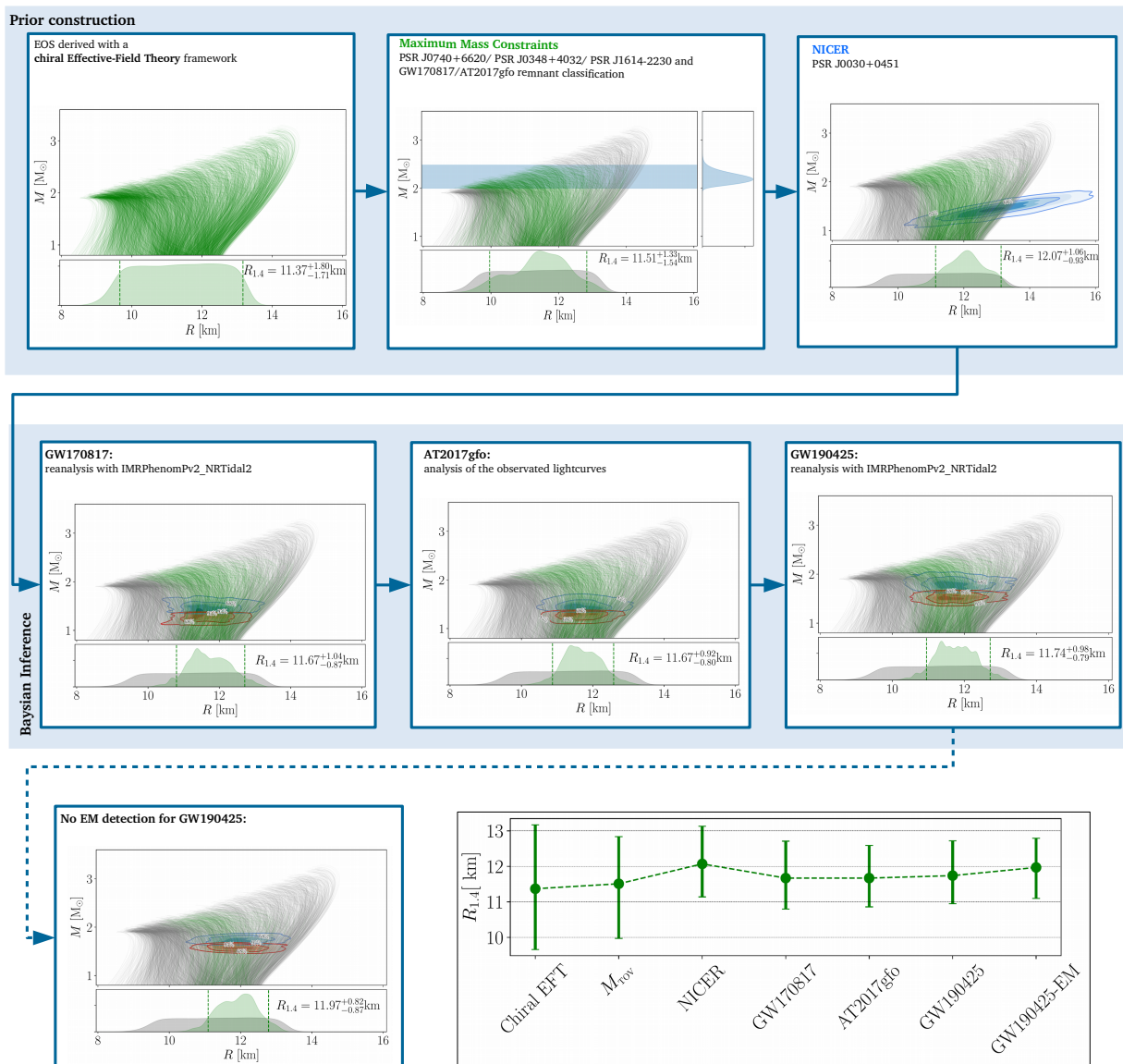


FIG. 1. Multi-step procedure to constrain the supranuclear EOS. We use a set of EOSs constrained by chiral EFT (top left panel). This EOS set is restricted (green EOSs are favored) by incorporating information of the mass measurements from PSR J0740+6620, PSR J0348+4032, PSR J1614-2230 and from the remnant classification of GW170817/AT2017gfo (middle top panel). The maximum mass posterior is shown in blue. We further restrict our EOS set by incorporating the NICER estimates of J0030+0451 (top right panel). This restricted set of EOSs is used to reanalyse GW170817 (first panel in the second row), where we show in the  $1\sigma$  and  $2\sigma$  contours for the primary star (blue) and the secondary star (red). We use the obtained results for the chirp mass, the mass ratio, and the EOS as a prior input to analyse AT2017gfo (middle panel in the second row). Finally, the obtained results are used as input for the analysis of GW190425 (right panel in the second row). Under the assumption that no EM signal was present for GW190425, we perform an analysis as for AT2017gfo (third row, left panel). At the bottom right, we show the radius constraint at every analysis steps. We mark (as in the other panels) the 90% confident intervals.

a  $1.4M_{\odot}$  NS is  $R_{1.4M_{\odot}} = 11.74^{+0.98}_{-0.79}$  km with 90% confidence.

To further enhance this analysis, it is possible to include the fact that no EM counterpart was detected for GW190425. This could be the result of EM searches not covering the necessary sky area or failing to reach the required sensitivity. We note, however, that a vari-

ety of EM follow-up searches were undertaken following this first BNS event in O3, including ATLAS, GOTO, the MASTER-network, and the Zwicky Transient Facility covering 37%, 30%, 37%, and 25% of the sky area, respectively. These follow-up campaigns have been performed independently, suggesting that in total a significant fraction of the sky area was covered. To include

Reference	EOS-method	Heavy PSRs	$M_{\max}$ (remnant)	GW1700817	AT2017gfo	GRB170817A	NICER	GW190425	$R_{1.4M_{\odot}}$
This work	chiral EFT	✓	✓	✓	✓	✓	✓	✓	$11.74^{+0.98}_{-0.79}$ km
Essick et al. [23]	chiral EFT	✓	✗	✓	✗	✗	✓	✗	$12.54^{+0.71}_{-0.63}$ km
Raaijmakers et al. [20]	chiral EFT	✓	✗	✓	✗	✗	✓	✗	[11.63, 13.26] km
Capano et al. [14]	chiral EFT	○	○	✓	✗	✗	✗	✗	$11.0^{+0.9}_{-0.6}$ km
Coughlin et al. [21]	-	✓	○	✓	✗	✗	✗	✗	[11.3; 13.5] km
Radice & Dai [13]	-	✗	✗	✓	○	✗	✗	✗	$(12.2^{+1.0}_{-0.8} \pm 0.2)$ km
LVC [11]	EOS paramet.	○	✗	✓	✗	✗	✗	✗	$11.9^{+1.4}_{-1.4}$ km
De et al. [10]	quasi-univ.	○	✗	✓	✗	✗	✗	✗	[8.9; 13.2] km
Annala et al. [9]	chiral EFT	○	✗	○	✗	✗	✗	✗	[9.9; 13.6] km

TABLE I. Overview of some of the published radius constraints from multi-messenger observations. We indicate if a particular work included constraints from heavy-pulsar mass measurements (Heavy PSRs), maximum-mass constraints obtained from the remnant classification of GW170817 ( $M_{\max}$ ), GW constraints from GW170817 or GW190425, constraints from kilonova lightcurves (AT2017gfo), constraints from the GRB afterglow (GRB170817A), and constraints from NICER. We refer to ✓ if either the full posterior or a Bayesian Inference has been part of the study, ○ refers to the inclusion of some astrophysical information without performing a Bayesian analysis or including the full posterior of other studies, and ✗ indicates that this information was not included in the study.

the ‘non-observation’, we employ the same kilonova analysis as presented before, where we use a combination of the apparent magnitude limits from optical surveys mentioned above. Together with the distance information from the GW skymap we obtain limits on the absolute magnitude of a potential counterpart. Using our lightcurve models, we rule out parts of the parameter space for which the predicted absolute magnitude would be above the obtained limit. Following the procedure, we arrive at a radius estimate of  $R_{1.4M_{\odot}} = 11.97^{+0.82}_{-0.87}$  km under the assumption that no detectable EM signal was produced for GW190425.

We compare our final result of  $R_{1.4M_{\odot}} = 11.74^{+0.98}_{-0.79}$  km which does not include the non-EM detection of GW190425, with a selection of previous influential studies in the literature in Tab. I. While our final result on the NS radius improved only slightly with respect to most previous studies, it has the advantage that it includes simultaneously information from GW170817, AT2017gfo, GRB170817A, GW190425, the NICER observation of PSR J0030+0451, and the radio observations of PSR J0740+6620, PSR J0348+4032, PSR J1614-2230. Furthermore, it is of particular importance that, as shown in the bottom right panel of Fig. 1, the inclusion of additional astrophysical observations does not necessarily lead to tighter constraints once (i) the full posteriors are incorporated in the analysis and (ii) the number of multi-messenger observations is very small.

Overall, our approach is general and conservative and can easily be extended to include new observations. Furthermore, it allows for strong phase transitions, the combination of multiple events, and even the incorporation of non-EM detections. Hence, our work paves the way for future multi-messenger analyses.

Our study of GW170817 and AT2017gfo does not

only provide insights into the composition of the NS interior and the NS radius, but also an independent measurement of the Hubble constant. This can be obtained by assuming that measurable properties related to the time-scale and color evolution of the ejecta are connected to the intrinsic luminosity of the kilonova. References [7, 40] recently showed that theoretical kilonova predictions can be used to standardize kilonovae lightcurves and thereby measure their distances. Combining the distance measurement with the redshift of the host constrains the Hubble constant [4]. For this purpose, we can combine the distance and inclination measurement of the GW (green contour in Fig. 2) and kilonova analysis (red contour in Fig. 2). We find that the particular constraint arising from the kilonova observation is not very tight, which is caused by the increased complexity of our lightcurve model compared to previous works. In the supplementary material, we show the consistency with two other kilonova models that suggests that our constraints are conservative. However, given that only one well-sampled kilonova has been detected, further observations are needed to test the robustness of different kilonova models in general. In addition, we include the inclination-distance measurement of the Very Long Baseline Interferometry (VLBI) of the GRB afterglow lightcurve as presented in Ref. [5]. Ref. [5] used three different models for the analysis and found that extracted results agreed within the stated uncertainties. Combining all measurements leads to an improved distance measurement, which can be related to an estimate of the Hubble constant of  $H_0 = 66.2^{+4.4}_{-4.2}$  km/Mpc/s at  $1\sigma$  uncertainty, cf. Fig. 2. We find that the inclusion of the VLBI measurement reduces the existing uncertainty on the Hubble constant much more than the kilonova measurement, but we point

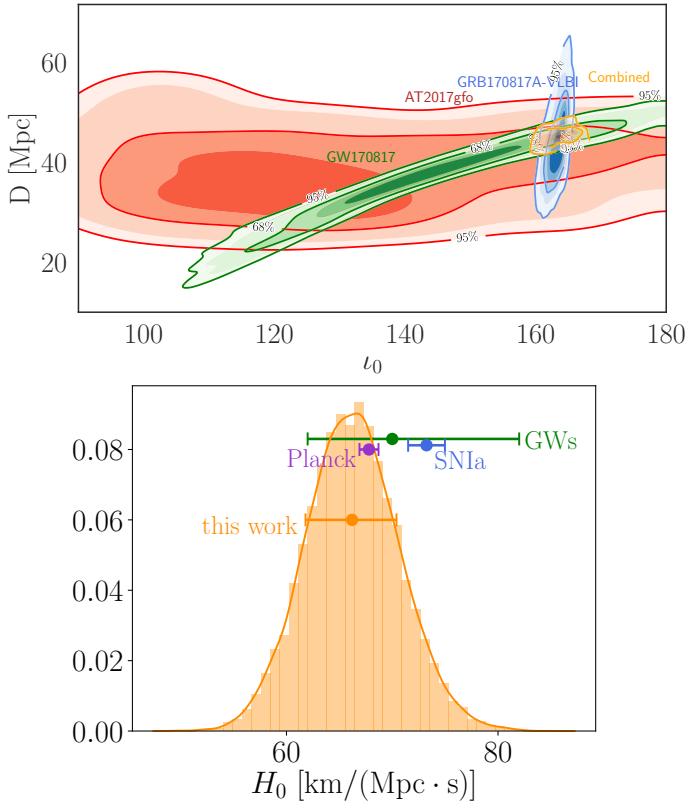


FIG. 2. Top panel: Estimated distance and inclination from the GW170817 (green) and AT2017gfo analysis (red) together with the VLBI constraint from [5] derived from GRB170817A (blue). The combined distance-inclination measurement is shown in orange. Bottom panel: Hubble constant estimate from our combined inclination measurement (orange), we also mark the  $1\sigma$  results of our study, the Planck measurement [38] (purple), the  $H_0$  measurement related to the distance ladder [39] (blue), and the  $H_0$ -estimate from GW170817 as in [4] (green).

out that while this is true for this single event, future GW detections might not have a visible GRB-afterglow due to restricted viewing angle of these events. Instead,

almost isotropic kilonovae might be observable. Thus, the possibility to combine different messengers in a flexible framework, as the one developed here, will be of advantage with an increasing number of detected compact binary mergers. For our analysis, based on only one event, the final uncertainty is too large to solve the tension between measurements via the local distance ladder [39] and the Cosmic Microwave Background [38], but our results indicate a preference for the Planck data. In the future, due to an increasing number of detections of multi-messenger signals, the measurement uncertainty will decrease and our framework might be able to resolve the existing Hubble

## ACKNOWLEDGMENTS

We thank Kenta Hotokezaka for providing the posterior samples of [5]. We are also grateful to Zoheyr Doctor, Reed Essick, and the anonymous referees for helpful comments on the manuscript. TD acknowledges support by the European Union’s Horizon 2020 research and innovation program under grant agreement No 749145, BNS-mergers. PTHP is supported by the research program of the Netherlands Organization for Scientific Research (NWO). I.T. is supported by the U.S. Department of Energy, Office of Science, Office of Nuclear Physics, under contract No. DE-AC52-06NA25396, by the LDRD program at LANL, and by the NUCLEI SciDAC program. SA is supported by the CNES Postdoctoral Fellowship at Laboratoire Astroparticule et Cosmologie. Computations have been performed on the Minerva HPC cluster of the Max-Planck-Institute for Gravitational Physics and on SuperMUC-NG (LRZ) under project number pn56zo. Computational resources have also been provided by the Los Alamos National Laboratory Institutional Computing Program, which is supported by the U.S. Department of Energy National Nuclear Security Administration under Contract No. 89233218CNA000001, and by the National Energy Research Scientific Computing Center (NERSC), which is supported by the U.S. Department of Energy, Office of Science, under contract No. DE-AC02-05CH11231.

[1] B. P. Abbott, *et al.*, *Phys. Rev. Lett.* **119**, 161101 (2017).  
 [2] B. P. Abbott, *et al.*, *Astrophys. J.* **848**, L13 (2017).  
 [3] B. Abbott, *et al.*, *Astrophys. J. Lett.* **848**, L12 (2017).  
 [4] B. P. Abbott, *et al.*, *Nature*, 10.1038/nature24471 (2017).  
 [5] K. Hotokezaka, *et al.*, *Nature Astron.* (2019).  
 [6] M. Fishbach, *et al.*, *Astrophys. J.* **871**, L13 (2019).  
 [7] M. W. Coughlin, *et al.*, *Phys. Rev. Research.* **2**, 022006 (2020).  
 [8] S. Dhawan, M. Bulla, A. Goobar, A. S. Carracedo, C. N. Setzer, *arXiv e-prints* p. 1909.13810 (2019).

[9] E. Annala, T. Gorda, A. Kurkela, A. Vuorinen, *Phys. Rev. Lett.* **120**, 172703 (2018).  
 [10] S. De, *et al.*, *Phys. Rev. Lett.* **121**, 091102 (2018).  
 [11] B. P. Abbott, *et al.*, *Phys. Rev. Lett.* **121**, 161101 (2018).  
 [12] M. W. Coughlin, *et al.*, *Monthly Notices of the Royal Astronomical Society* **480**, 3871 (2018).  
 [13] D. Radice, L. Dai, *Eur. Phys. J.* **A55**, 50 (2019).  
 [14] C. D. Capano, *et al.*, *Nature Astronomy* (2019).  
 [15] B. Abbott, *et al.*, *Astrophys. J. Lett.* **892**, L3 (2020).  
 [16] M. W. Coughlin, *et al.*, *Mon. Not. Roy. Astron. Soc.* **492**, 863 (2020).  
 [17] M. C. Miller, *et al.*, *Astrophys. J. Lett.* **887**, L24 (2019).

- [18] T. E. Riley, *et al.*, *Astrophys. J. Lett.* **887**, L21 (2019).
- [19] G. Raaijmakers, *et al.*, *Astrophys. J. Lett.* **887**, L22 (2019).
- [20] G. Raaijmakers, *et al.*, *Astrophys. J. Lett.* **893**, L21 (2020).
- [21] M. W. Coughlin, T. Dietrich, B. Margalit, B. D. Metzger, *Monthly Notices of the Royal Astronomical Society: Letters* **489**, L91 (2019).
- [22] J.-L. Jiang, S.-P. Tang, Y.-Z. Wang, Y.-Z. Fan, D.-M. Wei, *Astrophys. J.* **892**, 1 (2020).
- [23] R. Essick, I. Tews, P. Landry, S. Reddy, D. E. Holz, *arxiv:2004.07744* (2020).
- [24] T. Dietrich, *et al.*, *Phys. Rev.* **D100**, 044003 (2019).
- [25] M. Bulla, *Mon. Not. Roy. Astron. Soc.* **489**, 5037 (2019).
- [26] K. Kiuchi, K. Kyutoku, M. Shibata, K. Taniguchi, *Astrophys. J.* **876**, L31 (2019).
- [27] E. Epelbaum, H.-W. Hammer, U.-G. Meißner, *Rev. Mod. Phys.* **81**, 1773 (2009).
- [28] J. Carlson, *et al.*, *Rev. Mod. Phys.* **87**, 1067 (2015).
- [29] J. A. Melendez, S. Wesolowski, R. J. Furnstahl, *Phys. Rev.* **C96**, 024003 (2017).
- [30] I. Tews, J. Carlson, S. Gandolfi, S. Reddy, *Astrophys. J.* **860**, 149 (2018).
- [31] I. Tews, J. Margueron, S. Reddy, *Phys. Rev.* **C98**, 045804 (2018).
- [32] L. Rezzolla, E. R. Most, L. R. Weih, *Astrophys. J.* **852**, L25 (2018).
- [33] H. T. Cromartie, *et al.*, *Nature Astron.* **4**, 72 (2019).
- [34] J. Antoniadis, *et al.*, *Science* **340**, 6131 (2013).
- [35] Z. Arzoumanian, *et al.*, *Astrophys. J. Suppl.* **235**, 37 (2018).
- [36] R. Smith, G. Ashton, *arxiv:1909.11873* (2019).
- [37] B. P. Abbott, *et al.*, *Phys. Rev.* **X9**, 011001 (2019).
- [38] P. A. R. Ade, *et al.*, *Astron. Astrophys.* **594**, A13 (2016).
- [39] A. G. Riess, *et al.*, *Astrophys. J.* **826**, 56 (2016).
- [40] R. Kashyap, G. Raman, P. Ajith, *Astrophys. J.* **886**, L19 (2019). [*Astrophys. J. Lett.*886,L19(2019)].
- [41] LIGO Scientific Collaboration, Virgo Collaboration, <https://www.gw-openscience.org/events/GW170817/> (2017).
- [42] LIGO Scientific Collaboration, Virgo Collaboration, [https://www.gw-openscience.org/eventapi/html/03\\_Discovery\\_Papers/GW190425/v1/](https://www.gw-openscience.org/eventapi/html/03_Discovery_Papers/GW190425/v1/) (2020).
- [43] S. Weinberg, *Phys.Lett.* **B251**, 288 (1990).
- [44] S. Weinberg, *Nucl.Phys.* **B363**, 3 (1991).
- [45] U. van Kolck, *Phys. Rev.* **C49**, 2932 (1994).
- [46] R. Machleidt, D. R. Entem, *Phys. Rept.* **503**, 1 (2011).
- [47] E. Epelbaum, H. Krebs, U.-G. Meißner, *Eur. Phys. J. A* **51**, 53 (2015).
- [48] I. Tews, Z. Davoudi, A. Ekström, J. D. Holt, J. E. Lynn, *arxiv:2001.03334* (2020).
- [49] A. Gezerlis, *et al.*, *Phys. Rev. Lett.* **111**, 032501 (2013).
- [50] A. Gezerlis, *et al.*, *Phys. Rev. C* **90**, 054323 (2014).
- [51] J. E. Lynn, *et al.*, *Phys. Rev. Lett.* **116**, 062501 (2016).
- [52] J. E. Lynn, I. Tews, S. Gandolfi, A. Lovato, *Ann. Rev. Nucl. Part. Sci.* **69**, 279 (2019).
- [53] I. Tews, *Phys. Rev.* **C95**, 015803 (2017).
- [54] I. Tews, J. Margueron, S. Reddy, *Eur. Phys. J. A* **55**, 97 (2019).
- [55] S. Greif, G. Raaijmakers, K. Hebeler, A. Schwenk, A. Watts, *Mon. Not. Roy. Astron. Soc.* **485**, 5363 (2019).
- [56] K. Hebeler, J. Lattimer, C. Pethick, A. Schwenk, *Astrophys. J.* **773**, 11 (2013).
- [57] D. Alvarez-Castillo, S. Benic, D. Blaschke, S. Han, S. Typel, *Eur. Phys. J. A* **52**, 232 (2016).
- [58] M. C. Miller, C. Chirenti, F. K. Lamb, *arxiv:1904.08907* (2019).
- [59] B. Margalit, B. D. Metzger, *Astrophys. J.* **850**, L19 (2017).
- [60] M. Shibata, E. Zhou, K. Kiuchi, S. Fujibayashi, *Phys. Rev.* **D100**, 023015 (2019).
- [61] S. Bogdanov, *et al.*, *Astrophys. J.* **887**, L26 (2019).
- [62] The samples have been downloaded from <https://zenodo.org/record/3473466#.XiBajeZKiis>.
- [63] G. Ashton, *et al.*, *Astrophys. J. Suppl.* **241**, 27 (2019).
- [64] We use the public data released in Refs. [41, 42] for our reanalysis.
- [65] F. B. Farr, W. M., L. T., *Collaboration Technical Report* .
- [66] C. Cahillane, *et al.*, *Phys. Rev. D* **96**, 102001 (2017).
- [67] A. D. Viets, *et al.*, *Classical and Quantum Gravity* **35**, 095015 (2018).
- [68] N. J. Cornish, T. B. Littenberg, *Classical and Quantum Gravity* **32**, 135012 (2015).
- [69] T. B. Littenberg, N. J. Cornish, *Phys. Rev. D* **91**, 084034 (2015).
- [70] M. Hannam, *et al.*, *Phys. Rev. Lett.* **113**, 151101 (2014).
- [71] T. Dietrich, S. Bernuzzi, W. Tichy, *Phys. Rev.* **D96**, 121501 (2017).
- [72] T. Dietrich, *et al.*, *Phys. Rev.* **D99**, 024029 (2019).
- [73] B. P. Abbott, *et al.*, *Class. Quant. Grav.* **37**, 045006 (2020).
- [74] B. P. Abbott, *et al.*, *Phys. Rev.* **X9**, 031040 (2019).
- [75] B. P. Abbott, *et al.*, *Phys. Rev. Lett.* **123**, 011102 (2019).
- [76] D. Kasen, B. Metzger, J. Barnes, E. Quataert, E. Ramirez-Ruiz, *Nature*, [10.1038/nature24453](https://doi.org/10.1038/nature24453) (2017).
- [77] J. Barnes, D. Kasen, M.-R. Wu, G. Martínez-Pinedo, *Astrophys. J.* **829**, 110 (2016).
- [78] T. Dietrich, M. Ujevic, *Class. Quant. Grav.* **34**, 105014 (2017).
- [79] A. Perego, D. Radice, S. Bernuzzi, *Astrophys. J.* **850**, L37 (2017).
- [80] K. Kawaguchi, M. Shibata, M. Tanaka, *The Astrophysical Journal* **889**, 171 (2020).
- [81] The dynamical ejecta used here is essentially a high-velocity portion of the geometry adopted in Ref. [25].
- [82] I. Andreoni, *et al.*, *Publ. Astron. Soc. Austral.* **34**, e069 (2017).
- [83] I. Arcavi, *et al.*, *Nature* **551**, 64 (2017).
- [84] R. Chornock, *et al.*, *Astrophys. J. Lett.* **848**, L19 (2017).
- [85] P. S. Cowperthwaite, *et al.*, *Astrophys. J.* **848**, L17 (2017).
- [86] M. Drout, *et al.*, *Science* **358**, 1570 (2017).
- [87] P. Evans, *et al.*, *Science* **358**, 1565 (2017).
- [88] M. M. Kasliwal, *et al.*, *Science* **358**, 1559 (2017).
- [89] N. R. Tanvir, *et al.*, *Astrophys. J.* **848**, L27 (2017).
- [90] E. Pian, *et al.*, *Nature* **551**, 67 (2017).
- [91] E. Troja, *et al.*, *Nature*:[24290](https://doi.org/10.1038/nature24290) (2017).
- [92] S. J. Smartt, *et al.*, *Nature*, [10.1038/nature24303](https://doi.org/10.1038/nature24303) (2017).
- [93] Y. Utsumi, *et al.*, *Publ. Astron. Soc. Jap.* **69**, 101 (2017).
- [94] S. Valenti, *et al.*, *Astrophys. J.* **848**, L24 (2017).

- [95] Z. Doctor, B. Farr, D. E. Holz, M. Puerrer, *Phys. Rev.* **D96**, 123011 (2017).
- [96] M. Pürrer, *Class. Quant. Grav.* **31**, 195010 (2014).
- [97] O. McBrien, *et al.*, *GRB Coordinates Network* **24197**, 1 (2019).
- [98] B. P. Gompertz, *et al.*, *arxiv:2004.00025* (2020).
- [99] V. Lipunov, *et al.*, *GRB Coordinates Network* **24167**, 1 (2019).
- [100] M. W. Coughlin, *et al.*, *Astrophys. J. Lett.* **885**, L19 (2019).
- [101] D. Radice, *et al.*, *Astrophys. J.* **869**, 130 (2018).
- [102] T. Dietrich, M. Ujevic, W. Tichy, S. Bernuzzi, B. Brügmann, *Phys. Rev.* **D95**, 024029 (2017).
- [103] K. Hotokezaka, K. Kyutoku, H. Okawa, M. Shibata, K. Kiuchi, *Phys.Rev.* **D83**, 124008 (2011).
- [104] M. Agathos, *et al.*, *Phys. Rev. D* **101**, 044006 (2020).
- [105] G. Hinshaw, *et al.*, *apjs* **180**, 225 (2009).
- [106] A. C. Crook, *et al.*, *apj* **655**, 790 (2007).
- [107] C. M. Springob, *et al.*, *mnras* **445**, 2677 (2014).
- [108] J. Carrick, S. J. Turnbull, G. Lavaux, M. J. Hudson, *Monthly Notices of the Royal Astronomical Society* **450**, 317–332 (2015).
- [109] This choice of selection effect term is rooted to a volumetric prior on redshift [4].
- [110] D. Foreman-Mackey, D. W. Hogg, D. Lang, J. Goodman, *PASP* **125**, 306 (2013).

## SUPPLEMENTARY MATERIALS

### Chiral effective-field theory and the neutron-star equation of state

From a microscopic viewpoint, nuclear interactions are governed by a multitude of processes, e.g., various longer-range meson-exchanges between two or more nucleons or short-range processes that are typically modeled by contact interactions. Given this large number of operator structures for nuclear interactions, a guiding principle which arranges these operators according to their importance is desirable. Nuclear effective field theories (EFT), like chiral EFT [27, 43–46], allow us to do that.

Nuclear EFTs start from the most general Lagrangian that is consistent with all symmetries of the fundamental theory of strong interactions, Quantum Chromodynamics, and that describes the various interaction mechanisms. In chiral EFT, this Lagrangian is written in terms of nucleon and pion degrees of freedom, and includes pion-exchange interactions as well as nucleon-contact interactions. The latter absorb short-range effects, e.g., exchanges of heavier mesons, and depend on coupling constants that have to be adjusted to experimental data. Since this Lagrangian contains an infinite number of terms, it is then expanded in powers of momenta  $p$  over the so-called breakdown scale  $\Lambda_b$ . In addition to two-nucleon interactions, the chiral EFT expansion naturally includes also many-body forces, where three or more nucleons interact with each other. The result of this approach is a systematic and consistent expansion of two- and many-body nuclear forces, which can be truncated at a given order, allows for nuclear interactions to be systematically improved, and enables theoretical uncertainty estimates due to our incomplete understanding of nuclear interactions, see, e.g., Ref. [47].

As stated above, the determination of unknown coupling constants is performed by fitting the nuclear Hamiltonians order-by-order to experimental data. Usually, two-nucleon interactions are fit to two-nucleon scattering data, while many-body forces are adjusted in few- or many-body systems. However, new fitting protocols and other improvements are explored by the community, e.g., [48].

Chiral interactions allow a meaningful extrapolation of nuclear interactions away from experimentally accessible systems to systems that are difficult or impossible to measure in terrestrial laboratories, e.g., the neutron-rich matter in the core of NSs. However, chiral interactions are limited to momenta  $p < \Lambda_b \approx 600$  MeV [29]. At larger momenta, chiral interactions are not reliable because short-range (high-energy) physics that was absorbed by the coupling constants becomes important and needs to be explicitly included.

The EOSs used in this work are constrained at low densities by quantum Monte Carlo calculations of neutron matter [28], in particular with the auxiliary field diffusion Monte Carlo approach, using chiral interactions in their local formulation of Refs. [49–51]. These interactions were fit to two-nucleon scattering data, the  ${}^4\text{He}$  ground state energy, and neutron- $\alpha$  scattering phase shifts. A recent review of this approach can be found in Ref. [52]. In the past, we have analyzed the order-by-order convergence of this approach and found that it remains reasonable up to densities of twice the nuclear saturation density [23, 30]. To be more conservative, here we employ these constraints up to densities of  $1.5 n_{\text{sat}}$ .

These results, together with their uncertainty bands, allow us to constrain the NS EOS below  $1.5 n_{\text{sat}}$ . First, we extend the results to matter in  $\beta$ -equilibrium and add a crust [53]. We extend our EOS models to densities beyond  $1.5 n_{\text{sat}}$  by employing a model-agnostic parametric expansion scheme that represents the EOS in the speed of sound plane [14, 31, 54, 55]. In particular, we sample a set of six randomly distributed points  $c_s^2(n)$  between  $1.5 n_{\text{sat}}$  and  $12 n_{\text{sat}}$  and connect them by line segments. We found that NS properties are not very sensitive to the number of line segments when varying it between 5–10. This construction by design respects causality and stability,  $0 \leq c_s \leq c$ , with the speed of light  $c$ . For each sampled EOS, we construct a second EOS that includes a segment with  $c_s = 0$  with random onset density and width, to simulate EOS with strong first-order phase transitions.

Similar to commonly used polytropic expansion schemes [56], the speed-of-sound extension does not make any assumptions about degrees of freedom at higher densities, and includes many possible density dependencies for the EOS at high densities. For example, this extension includes regions of sudden stiffening or sudden softening, as would be expected from a strong first-order phase transition. From the speed-of-sound curve, we reconstruct the EOS and solve the Tolman-Oppenheimer-Volkoff equations to extract NS structure properties. In this work, we have sampled 5000 different EOS that give a uniform prior on the radius of a typical  $1.4 M_\odot$  NS.

### Incorporation of the maximum mass neutrons star constraints

For our inclusion of the astronomical constraints on the EOSs, we adopt a Bayesian approach and follow methods outlined in Refs. [23, 57, 58]. In particular, we express the constraints in terms of likelihood functions that can be used for the GW and EM analysis.

Pulsar	$M^{\text{PSR}} [M_{\odot}]$	$\sigma^{\text{PSR}} [M_{\odot}]$	Reference
PSR J0740+6620	2.14	0.1	[33]
PSR J0348+4032	2.01	0.04	[34]
PSR J1614-2230	1.908	0.016	[35]

TABLE II. The mass measurements and the  $1\text{-}\sigma$  error bound reported for the pulsars included for this analysis.

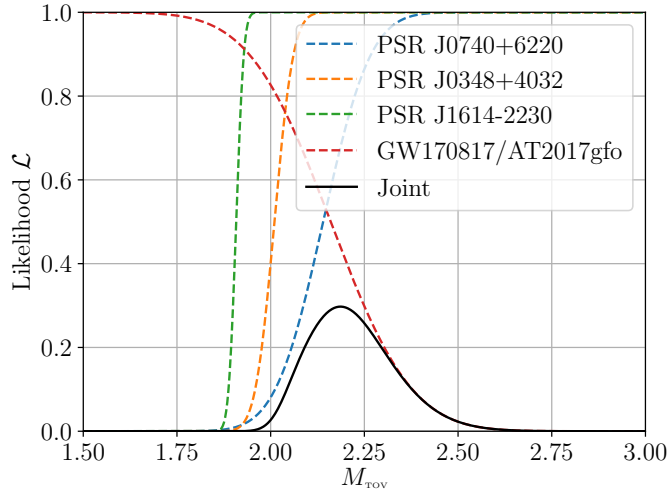


FIG. 3. Combined likelihood of the maximum mass by incorporating the constraints from radio observations of PSR J0740+6620 [33], PSR J0348+4032 [34], and PSR J1614-2230 [35] (lower bound) and the remnant classification of GW170817/AT2017gfo as a black hole [32] (upper bound).

We have used the constraints on the lower bound of the maximum NS mass  $M_{\text{max}}$  given by the mass measurements of PSR J0740+6620 [33], PSR J0348+4032 [34], PSR J1614-2230 [35], and the constraint on the upper bound on  $M_{\text{max}}$  estimated in Ref. [32]. Similar upper bounds on  $M_{\text{max}}$  have also been obtained in different studies, e.g., Refs. [32, 59, 60]. The corresponding likelihood  $\mathcal{L}_{M_{\text{max}}}$  is given by

$$\begin{aligned}
 \mathcal{L}_{M_{\text{max}}}(\text{EOS}) &= \mathcal{L}_{M_{\text{max}}}(M_{\text{max}}) \\
 &= \prod_i \text{CDF}(M_{\text{max}}, \mathcal{N}(\mu = M_i^{\text{PSR}}, \sigma = \sigma_i^{\text{PSR}})) \\
 &\quad \times (1 - \text{CDF}(M_{\text{max}}, \mathcal{N}(\mu = 2.16M_{\odot}, \sigma = 0.17M_{\odot}))),
 \end{aligned} \tag{1}$$

where  $\text{CDF}(x, \mathcal{N}(\mu, \sigma))$  is the cumulative distribution function corresponding to a normal distribution  $\mathcal{N}(\mu, \sigma)$  evaluated at  $x$ .  $M_i^{\text{PSR}}$  and  $\sigma_i^{\text{PSR}}$  are the mass measurement and the  $1\text{-}\sigma$  error bound reported for the pulsars that we included for the analysis, respectively. The values for  $M_i^{\text{PSR}}$  and  $\sigma_i^{\text{PSR}}$  are tabulated in Tab. II. For the upper bound on  $M_{\text{max}}$ , we take a more conservative error and, hence, use the 90% credible range as the standard deviation for the likelihood input. In the above likelihood  $\mathcal{L}_{\text{TOV}}$ , we have approximated the measurement and estimates reported in Refs. [33–35] and [32] to be Gaussian. The final likelihood is shown in Fig. 3.

### Coherent incorporation of NICER data

For the NICER data [61], we use the results presented in Ref. [17] where a Bayesian inference approach was used to analyze the energy-dependent thermal X-ray waveform of PSR J0030+0451. Our study employs the publicly available samples obtained with the best-fit approximant of [17], namely a three-oval, uniform-temperature spots model[62]. This model provides excellent agreement with the observed NICER data and allows to infer the mass and radius of PSR J0030+0451 to be  $M = 1.44^{+0.15}_{-0.14}M_{\odot}$  and  $R = 13.02^{+1.24}_{-1.06}\text{km}$  (both at  $1\sigma$  uncertainty). As pointed out in Refs. [17, 18] the inferred mass-radius relations are not dominated by systematic uncertainties and inferred parameters are in good agreement for different models; as a comparison the results for the two-oval spot model are

also shown in Fig. 1 (orange contours in the middle left panel). The corresponding likelihood  $\mathcal{L}_{\text{NICER}}$  is given by

$$\begin{aligned}\mathcal{L}_{\text{NICER}}(\text{EOS}) &= \int dM dR p_{\text{NICER}}(M, R) \pi(M, R | \text{EOS}) \\ &= \int dM dR p_{\text{NICER}}(M, R) \delta(R - R(M, \text{EOS})) \\ &= \int dM p_{\text{NICER}}(M, R = R(M, \text{EOS})),\end{aligned}\tag{2}$$

where  $p_{\text{NICER}}(M, R)$  is the joint-posterior of mass and radius of PSR J0030+0451 as measured by NICER and we use the fact that the radius is a function of mass for a given EOS.

As a result the joint constraint likelihood  $\mathcal{L}_{\text{Joint}}$  combining the maximum mass and the NICER information is given by

$$\mathcal{L}_{\text{Joint}}(\text{EOS}) = \mathcal{L}_{\text{NICER}} \times \mathcal{L}_{M_{\text{max}}}.\tag{3}$$

$\mathcal{L}_{\text{Joint}}$  is then taken as an input for our further analysis of GW170817, AT2017gfo, and GW190425.

### Gravitational-Wave Analysis

We use the `bilby` infrastructure [63] to reanalyze GW170817 and GW190425 [64]. With the help of `parallel bilby` [36] we can run on 800 compute cores to obtain final posteriors within a few hours on the HPC clusters Minerva at the Max-Planck-Institute for Gravitational Physics or on SuperMUC-NG at the Leibniz Supercomputing Centre. The GW signals are analysed within a frequency interval of  $f \in [23, 2048]$  Hz which covers the full inspiral of the BNS coalescence. Frequency-dependent spline calibration envelopes [65] are introduced into the waveform templates to counteract the potential systematics due to the uncertainties in the detectors' calibrations [66, 67]. We also use the power spectral density, which is used by the GW data analysis, estimated with `BayesWave` [68, 69].

We employ for the first time the new `IMRPhenomPv2_NRTidalv2` waveform model. The approximant augments the precessing binary black-hole waveform model [70] with the description outlined in Ref. [24]. `IMRPhenomPv2_NRTidalv2` has an improved tidal and spin description compared to the `IMRPhenomPv2_NRTidal` model [71, 72], which has been the standard waveform employed by the LIGO Scientific and Virgo Collaborations to interpret GW170817 [11, 37, 73–75] and GW190425 [15]. We present the parameter-estimation results of the most important parameters for our study in Fig. 4 for GW170817. For comparison, we also show the posteriors obtained with the `IMRPhenomPv2_NRTidal` (orange) waveform model to allow for an assessment of the usage of the improved waveform model `NRTidalv2` (blue). We find no noticeable difference in the measured component masses, distance and inclination. The very good agreement is likely caused by the same underlying point-particle base line of both models. But, we note a small difference in the estimated tidal deformability, where `NRTidalv2` predicts a slightly larger tidal deformability which consequently results in a slightly larger radius estimate. This behavior is expected since the `NRTidalv2` approximant incorporates slightly smaller tidal contributions for the same physical parameters than the original `NRTidal` model, which consequently leads to a larger estimated tidal deformability.

For the analysis of GW190425 we also use the `IMRPhenomPv2_NRTidalv2` model. In Fig. 5 we show important source parameters for GW190425 when we include/ not include the GW170817 and AT2017gfo information (chirp mass, mass ratio, and EOS constraints), i.e, the middle row of Fig. 1. The main difference is again visible in the estimated tidal deformability  $\tilde{\Lambda}$ , where the inclusion of GW170817 and AT2017gfo in our analysis leads to a smaller value of the tidal deformability. Overall, the incorporation of additional information from GW170817 and AT2017gfo changed the prior of the GW190425 analysis and NSs with too large radii (large tidal deformabilities) are already disfavored.

### AT2017gfo

#### *Kilonova modelling*

For the assessment of systematic uncertainties, we compare different lightcurve models mainly based on Refs. [25] and [76].

*Model I (standard model):* Here we use Spectral Energy Distributions (SEDs) simulated using the multi-dimensional Monte Carlo radiative transfer code `POSSIS` [25]. In particular, we present a new modelled grid that differs from the one in Ref. [25] in terms of the underlying physics and the assumed geometry for the ejecta. In terms of physics, there are

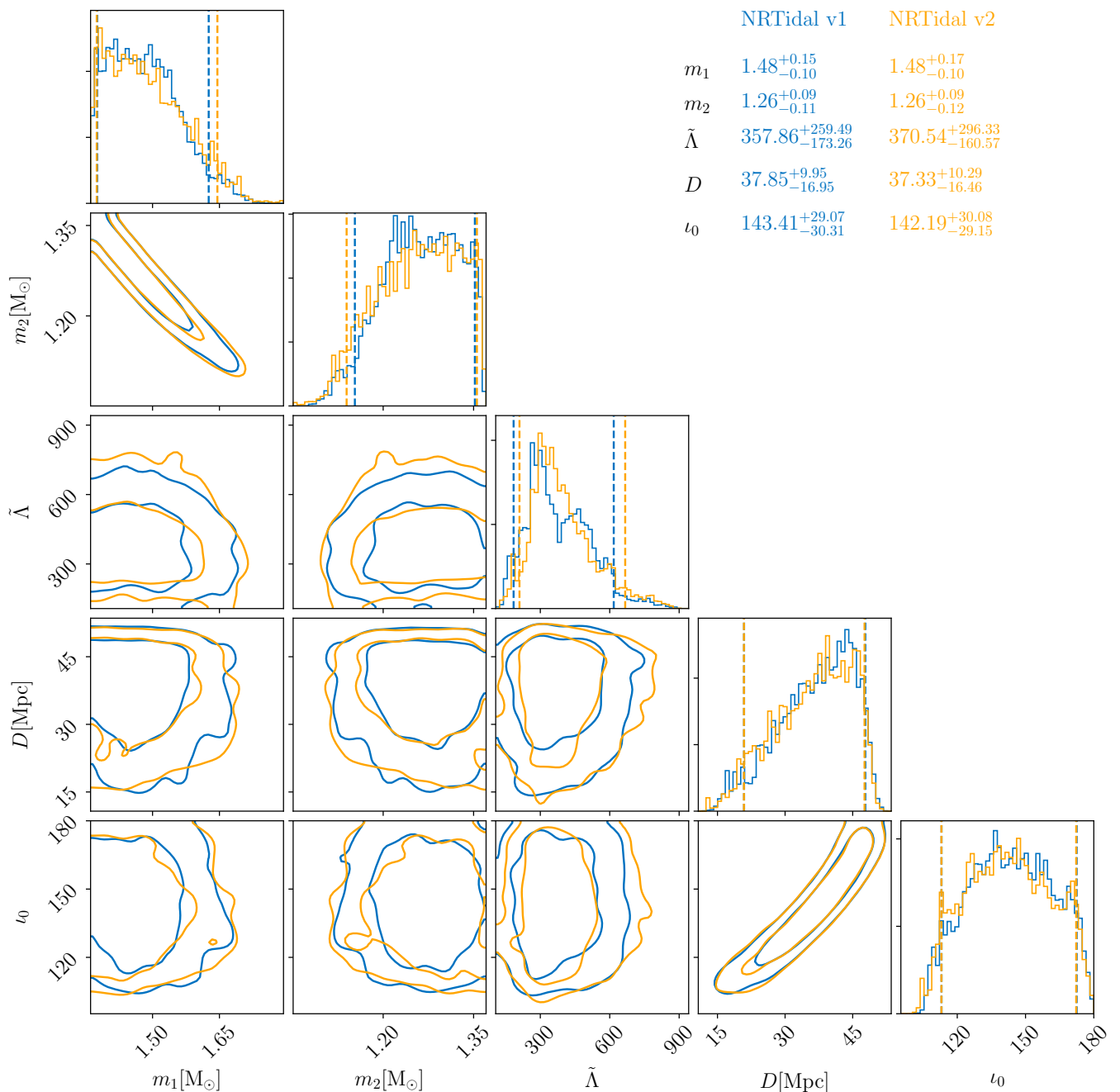


FIG. 4. Corner plot of the posterior distribution of GW170817’s parameters obtained with `IMRPhenomPv2_NRTidal` (blue) and `IMRPhenomPv2_NRTidalv2` (orange). The parameters shown are; primary source mass  $m_1$ , secondary source mass  $m_2$ , mass-weighted tidal deformability  $\tilde{\Lambda}$ , luminosity distance  $D$  and inclination  $i_0$ . The major difference between the posteriors inferred with the two waveform models is the distribution of  $\tilde{\Lambda}$ . This difference is expected as the tidal description of the two models are different.

two main differences compared to simulations presented in Ref. [25]: thermalization efficiencies are taken from Ref. [77] and the temperature is no longer parametrized and uniform throughout the ejecta but rather estimated in each grid cell and at each time from the mean intensity of the radiation field (inferred from the density and local energy deposition from radioactive decay). In terms of the adopted geometry, we run calculations for a geometry (Fig. 6) more similar to the one described in, e.g., Refs. [78–80] and obtained from numerical relativity simulations. A first component represents the dynamical ejecta, extending from  $v_{\min}^{\text{dyn}} = 0.08c$  to  $v_{\max}^{\text{dyn}} = 0.3c$ , characterised by an ejecta mass  $m_{\text{ej}}^{\text{dyn}}$  and with lanthanide-rich composition within an angle  $\pm\phi$  about the equatorial plane and lanthanide-free composition

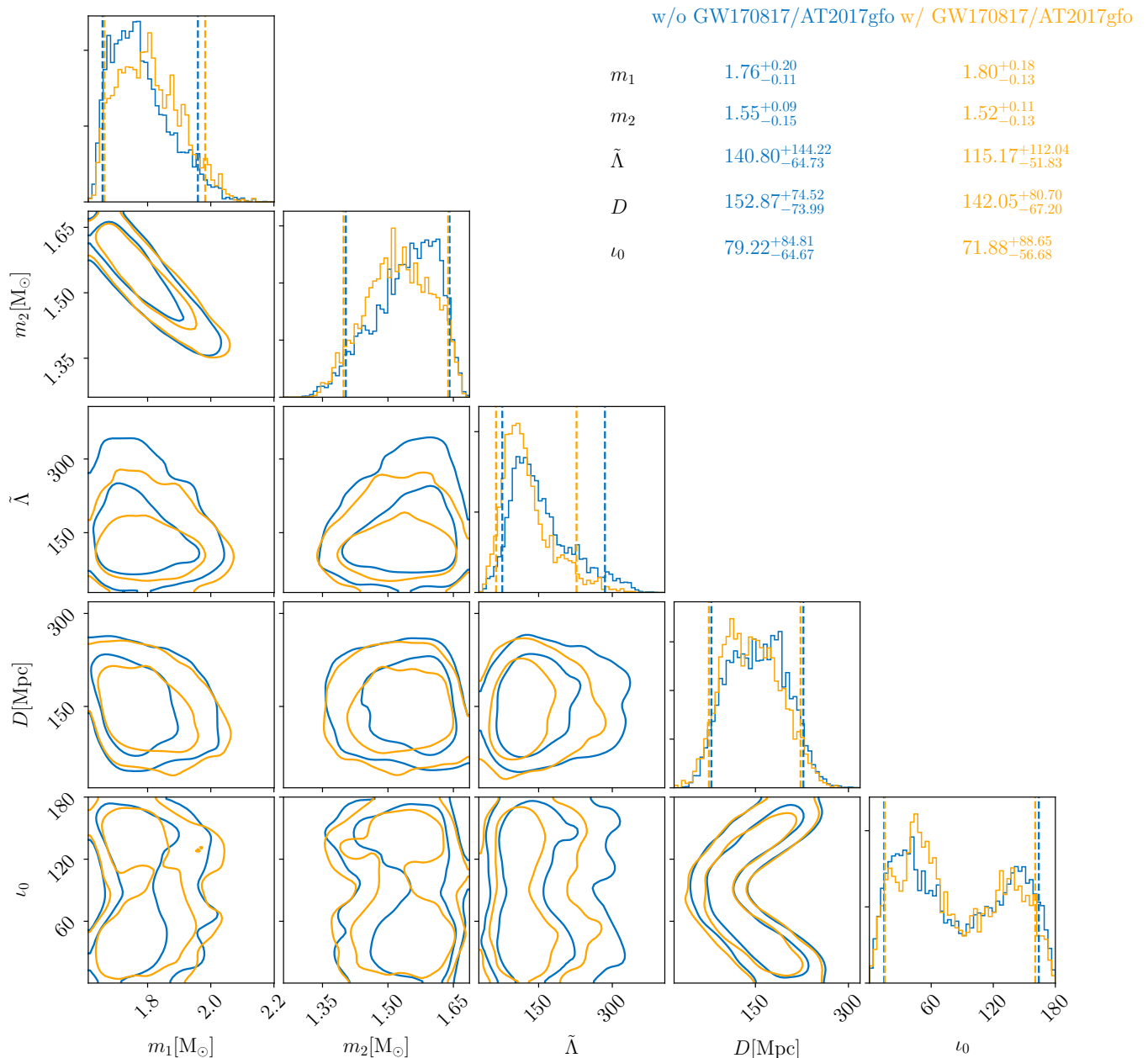


FIG. 5. Corner plot of the posterior distribution of GW190425’s parameters obtained without (blue) and with (orange) the inclusion of GW170817/AT2017gfo. The parameters shown are; primary source mass  $m_1$ , secondary source mass  $m_2$ , mass-weighted tidal deformability  $\tilde{\Lambda}$ , luminosity distance  $D$  and inclination  $i_0$ . With the inclusion of GW170817/AT2017gfo, the tidal measurement is more constrained.

otherwise[81]. The opacities assumed in the dynamical ejecta have the same wavelength- and time-dependence as in Ref. [25], with  $\kappa_{\text{bb}}[1\mu\text{m}, 1.5\text{d}] = 1\text{cm}^2\text{g}^{-1}$  for the lanthanide-rich and  $\kappa_{\text{bb}}[1\mu\text{m}, 1.5\text{d}] = 5 \times 10^{-3}\text{cm}^2\text{g}^{-1}$  for the lanthanide-free portion of the ejecta (see Ref. [25] for more details). A second spherical component represents the ejecta released from the merger remnant and debris disk, extending from  $v_{\text{min}}^{\text{pm}} = 0.025\text{c}$  up to  $v_{\text{max}}^{\text{pm}} = 0.08\text{c}$  and with an ejecta mass  $m_{\text{ej}}^{\text{pm}}$ . Opacities adopted for the postmerger ejecta are intermediate [79] to those in the lanthanide-rich and lanthanide-free components of the dynamical ejecta ( $\kappa_{\text{bb}}[1\mu\text{m}, 1.5\text{d}] = 0.1\text{cm}^2\text{g}^{-1}$ ). SEDs and corresponding lightcurves are then controlled by four parameters:  $m_{\text{ej}}^{\text{dyn}}$ ,  $m_{\text{ej}}^{\text{pm}}$ ,  $\phi$  and the observer viewing angle  $\theta_{\text{obs}}$ .

*Model II:* In addition to our updated kilonova model, we also include a version similar to the one in Ref. [25], i.e., a model without an additional wind ejecta component. This model has the advantage that a standardization

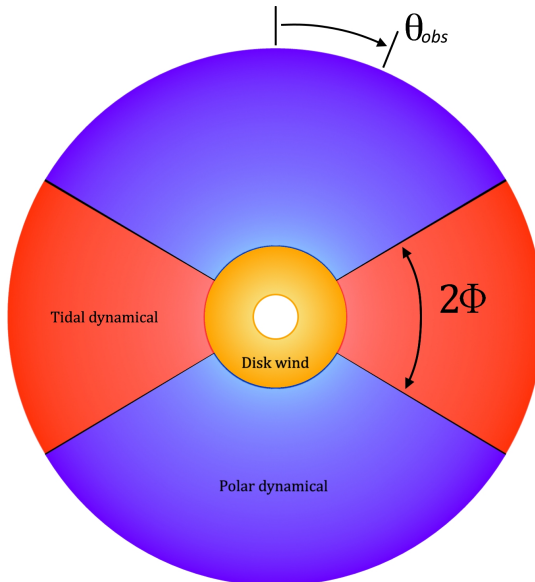


FIG. 6. Geometry employed in our Model I kilonova description, where different colors refer to the different lanthanide fractions of the individual ejecta components.

and therefore an extraction of the Hubble constant is easier due to the smaller number of free parameters and that therefore more tighter constraints on the distance and inclination angle are extracted compared to our standard choice (Model I); cf. Fig. 10.

*Model III:* As an alternative approach and to validate our results, we use the radiative transfer model of Ref. [76]. This model employs a multi-dimensional Monte Carlo code to solve the multi-wavelength radiation transport equation for an expanding medium. We assume one spherically symmetric ejecta component characterized by the mass of the ejecta  $m_{ej}$ , the mass fraction of lanthanides  $X_{lan}$ , and the ejecta velocity  $v_{ej}$ . While using only one ejecta component reduces the consistency between the observational data and the model prediction, it allows an easier standardization and therefore puts a tighter constraint on the measured distance, but no information about inclination can be extracted due to the assumption of spherical symmetry.

#### Surrogate Construction

In order to draw conclusions about generic sources, we use the approach outlined in Refs. [95, 96], where a Gaussian-Process-Regression framework is employed; cf. Refs. [12, 16] for a detailed discussion. We present the performance of our standard model (Model I) in Fig. 7 and find that it is capable of describing the observed data.

The extracted properties of the ejecta are shown in Fig. 8. We find that the disk wind ejecta is about 10 times larger than the dynamical ejecta, unfortunately, the angle  $\Phi$  (cf. Fig. 7) is not well constrained, while the observation angle  $\theta$  peaks around  $50^\circ$ .

To connect the individual ejecta components to the different ejecta mechanisms, we assume that the total ejecta mass is a sum of multiple components. The first component is related to the dynamical ejecta  $m_{ej}^{dyn}$ , i.e., to the material released during the merger process via shocks and torque. The second component is caused by disk wind ejecta and proportional to the disk mass surrounding the final remnant  $m_{ej}^{pm} = \zeta m_{disk}$ . To allow a conservative estimate, we also add a third component  $\alpha$  that we keep as a free parameter during the sampling procedure.

For the dynamical ejecta, we use the description in Ref. [21], while we assume that the disk wind ejecta is proportional to the disk mass. Based on recent works outlining potential issues of previous relations predicting the disk mass for systems with high mass ratios, we have extended previous studies to include an explicit mass-ratio dependence, see discussion below.

The extracted binary properties are shown in Fig. 9, in which we report the chirp mass, the mass ratio, the deformability  $\tilde{\Lambda}$ , the fraction of the dynamical ejecta  $\alpha$ , the disk conversion factor  $\zeta$ , and the maximum TOV mass. We point out that the tidal deformability and the maximum TOV-mass are just reported as a crosscheck and that the internal EOS index is used during the Bayesian Inference. Furthermore, we do find very good agreement between the three kilonova models. The biggest difference between all three models is visible in the measurement of the

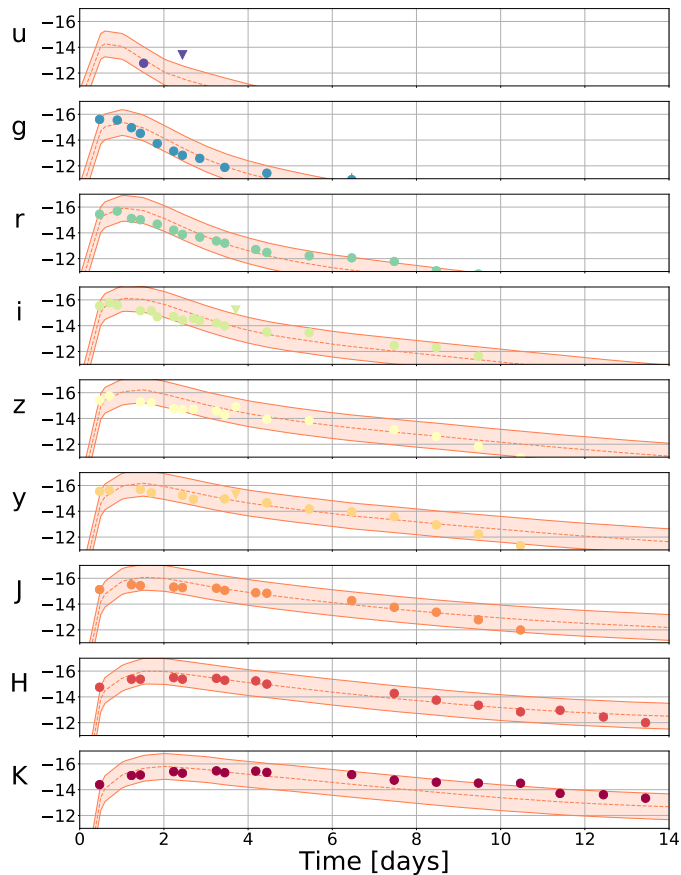


FIG. 7. Observed lightcurves of AT2017gfo in different bands and the predictions of Model I. Observational data are collected in [12] and are taken from [82–94].

inclination and distance. Therefore, we show the inclination-distance measurement in Fig. 10. Model I is the least constraining due to the fact that the additional wind ejecta component increases the complexity of the model and therefore makes a standardization more complicated, cf. Model II. Model III is spherical symmetric and therefore only allows a distance measurement. In summary, all three models agree within their statistical error estimates, which shows that our analysis is dominated by statistical effects rather than systematics.

For the analysis of the non-observed EM counterpart of GW190425, we use the same kilonova analysis as discussed above, but restrict ourselves to Model I as our standard model. In particular, we use information from ATLAS [97] that covered 37%, GOTO [98] that covered 30%, the MASTER-network [99] that covered 37%, and the Zwicky Transient Facility [100] that covered 25% of the GW sky area to obtain apparent magnitude limits on potential counterparts from optical surveys. Unfortunately, an exact computation of the total sky coverage is not possible since not all groups released their covered tiles and search information. However, the publicly known limits, together with the distance information from the GW event, lead to limits on the absolute magnitude of a potential kilonova; cf. [16] for further details and discussions. We rule out all ejecta parameters for which the predicted absolute magnitude would exceed the obtained absolute magnitude limit.

#### *New disk mass prediction*

We collect a set of results from 73 numerical relativity simulations performed by different groups [26, 101–103]. The full dataset is shown in Fig. 11 (left panel) in which we plot the disk mass versus the ratio of the total mass of the system and the threshold mass. The threshold mass determines when prompt collapse formation after the merger of the two stars happens. For the estimate of the threshold mass, we use the predictions of Ref. [104]. We compare the data with the estimate in Ref. [21] (solid black line) and it becomes evident that, as outlined in Ref. [26], an increasing mass ratio leads to an increased disk mass. To update the fit, we use a similar functional behavior as suggested in

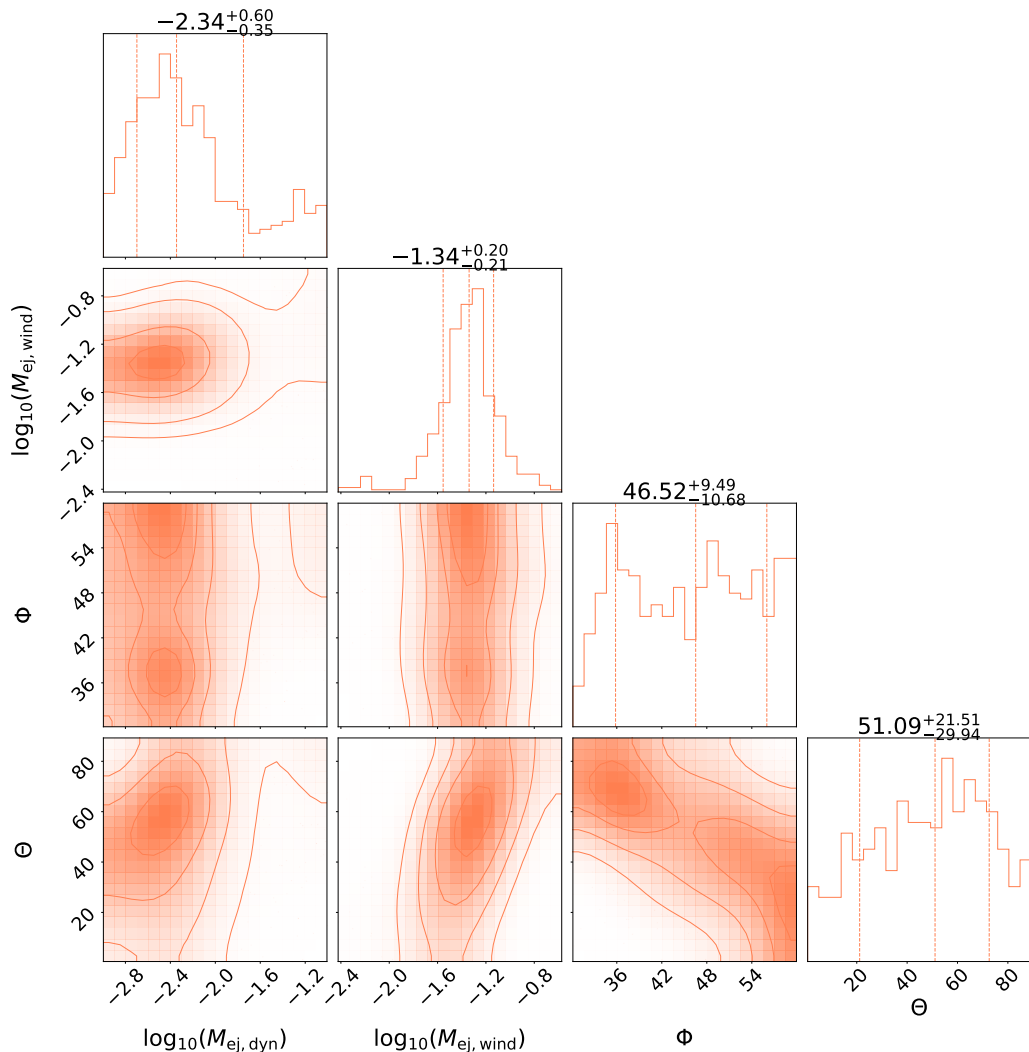


FIG. 8. Estimated ejecta parameters for Model I: the mass of the dynamical ejecta, the mass of the disk wind ejecta, the opening angle between lanthanide-rich and lanthanide-poor dynamical ejecta components, and the viewing angle.

Ref. [21], but we incorporate mass-ratio dependent fitting parameters that are obtained by minimizing

$$\log_{10}(M_{\text{disk}}) = \max\left(-3, a\left(1 + b \tanh\left(\frac{c - M/M_{\text{threshold}}}{d}\right)\right)\right), \quad (4)$$

with  $a$  and  $b$  given by

$$\begin{aligned} a &= a_o + \delta a \xi, \\ b &= b_o + \delta b \xi, \end{aligned} \quad (5)$$

where  $a_o$ ,  $b_o$ ,  $\delta a$  and  $\delta b$  are fitting coefficients and  $\xi$  is given by

$$\xi = \frac{1}{2} \tanh(\beta(q - q_{\text{trans}})). \quad (6)$$

The right panel of Fig. 11 shows how the fitting changes as the mass ratio changes. The plots shows that the updated fit is indeed able to capture the mass ratio dependence.

The best-fit parameters are given by minimizing  $r = \langle (\log_{10}(M_{\text{disk}}) - \log_{10}(M_{\text{disk}}^{\text{fit}}))^2 \rangle$ :  $a_o = -1.581$ ,  $\delta a = -2.439$ ,  $b_o = -0.538$ ,  $\delta b = -0.406$ ,  $c = 0.953$ ,  $d = 0.0417$ ,  $\beta = 3.910$ ,  $q_{\text{trans}} = 0.900$ .

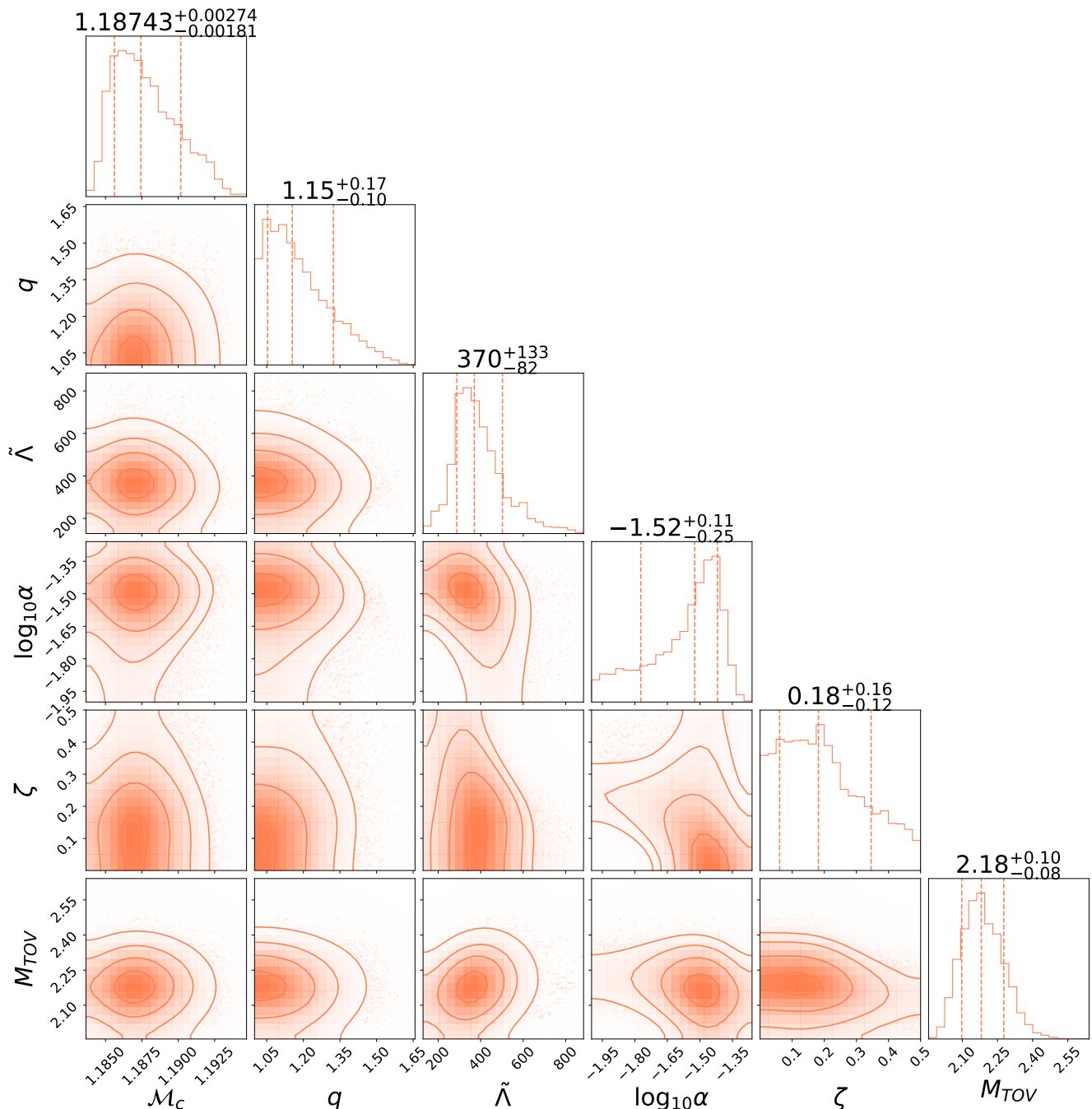


FIG. 9. Estimated parameters for Model I: chirp mass  $\mathcal{M}_c$ , mass ratio  $q$ , tidal deformability  $\tilde{\Lambda}$ , free ejecta parameter  $\alpha$ , disk conversion factor  $\zeta$ , and maximum NS mass. Model II and Model III provide very similar results with respect to the binary properties.

### Ordering of the analysis steps

To further increase the confidence in our framework, we present an alternative analysis with respect to Fig. 1 in which we simply exchange the ordering of the individual analysis steps, i.e., we include the NICER results at the end of our study. To reduce computational costs, we focus in this subsection only on the combination of GW170817, AT2017gfo, NICER, and the maximum-mass constraints. Fig. 12 shows our findings, where the green color indicates our original results of Fig. 1 and the blue color the analysis obtained within a different ordering (see top axis). As visible, the measured radius is slightly larger for our original analysis than for our analysis in which NICER results

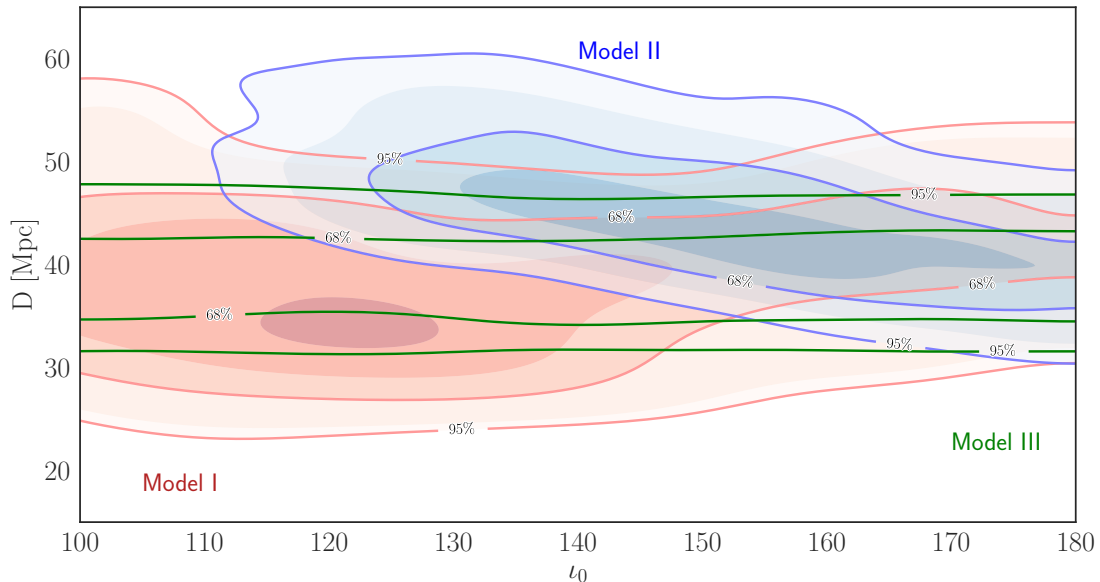


FIG. 10. Distance and inclination measurement for Model I, Model II, and Model III. Model I is the least constraining, but used within the main text since it allows the best physical description of the BNS merger and postmerger phase.

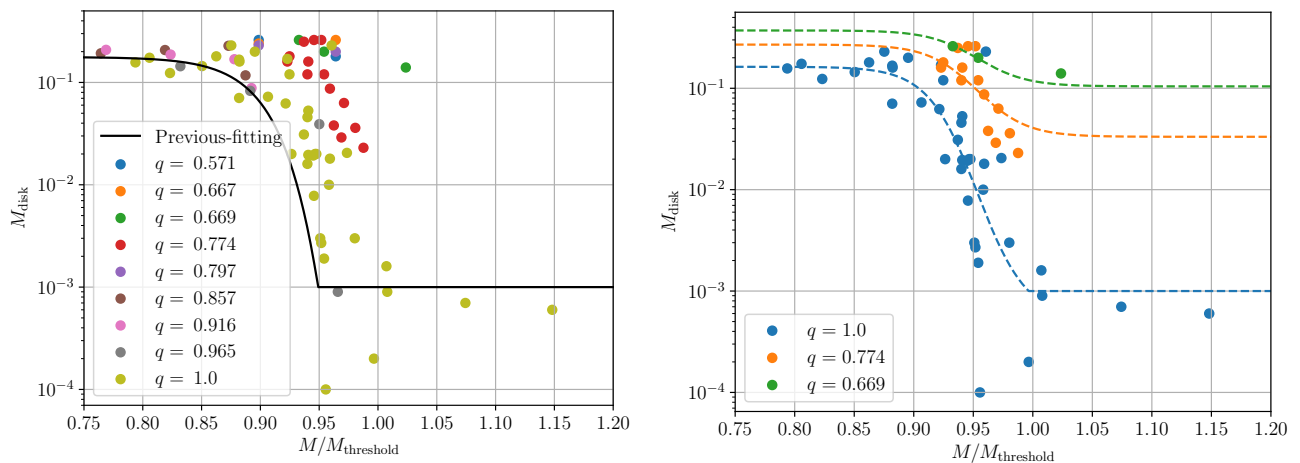


FIG. 11. Left panel: Data employed for the construction of the fit, Eq. (4), in comparison with the previous fit of [21]. Right panel: A few example cases for different mass ratios with the derived relation on top.

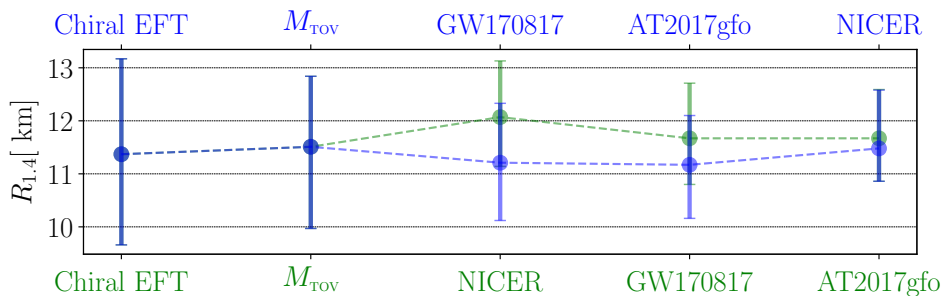


FIG. 12. Radius constraint under an interchange of the individual analysis steps.

are added at the end. This slight change is due to the kernel density estimation that is used to obtain the prior for our individual analysis steps. However, the 90% confidence intervals remain unchanged. This clearly proves the robustness of our method and the overall procedure.

### Prior combination for distance measurement

Due to the strong correlation between the luminosity distance  $D$  and inclination  $\iota_0$  inference across different analysis, we combine the information on the  $D$ - $\iota_0$  and then marginalize over the inclination. With Bayesian statistics in mind, we take the GRB170817A-VLBI measurement  $p_{\text{GRB}}(D, \iota_0)$  as the prior for the other two analysis. Therefore, the combined posterior  $p_{\text{com}}(D, \iota_0)$  is given by

$$p_{\text{com}}(D, \iota_0) = \mathcal{L}_{\text{GW}} \times \mathcal{L}_{\text{EM}} \times p_{\text{GRB}}(D, \iota_0), \quad (7)$$

where  $\mathcal{L}_{\text{GW}}$  and  $\mathcal{L}_{\text{EM}}$  are the likelihoods for the parameter  $(D, \iota_0)$  with GW170817 and AT2017gfo analysis, respectively.

Because we are combining the information in the post-processing stage, we do not have access to the likelihood but the posteriors of GW170817  $p_{\text{GW}}$  and AT2017gfo  $p_{\text{EM}}$  only. Therefore, we evaluate the combined posterior by

$$p_{\text{com}}(D, \iota_0) = \frac{p_{\text{GW}}}{\pi_{\text{GW}}} \times \frac{p_{\text{EM}}}{\pi_{\text{EM}}} \times p_{\text{GRB}}(D, \iota_0), \quad (8)$$

where  $\pi_{\text{GW}}$  and  $\pi_{\text{EM}}$  are the prior for the parameter  $(D, \iota_0)$  used for analysing GW170817 and AT2017gfo, respectively.

The combined posterior on the distance is then given by

$$p_{\text{com}}(D) = \int d\iota_0 p_{\text{com}}(D, \iota_0) \quad (9)$$

which can be later related to the Hubble constant measurement.

### Estimation of the Hubble constant $H_0$

The Hubble constant  $H_0$  relates the center-of-mass recession velocity relative to the CMB [105]  $v_r$  of a galaxy by

$$v_r = H_0 D_c + v_p, \quad (10)$$

where  $D_c$  and  $v_p$  are the comoving distance and the peculiar velocity, respectively. The distance between the Earth and GW170817 is small ( $\sim 40\text{Mpc}$ ), so that one can approximate the comoving distance with the luminosity distance  $D$ .

According to Ref. [106], the collection of galaxies to which GW170817's host galaxy NGC4993 belongs (ESO-508) has a radial velocity of  $v_r$  of  $3327 \pm 72\text{km s}^{-1}$  and according to Ref. [107] the peculiar velocity  $v_p$  of NGC4993 is  $310 \pm 69\text{ km s}^{-1}$ . In order to reduce the possible systematics introduced by the imperfectly modelling of the bulk flow motion in Ref. [107], we take the uncertainty on the  $v_p$  to be  $150\text{ km s}^{-1}$  [108].

We model the likelihood of  $v_r$ ,  $\mathcal{L}(v_r)$ , and  $v_p$ ,  $\mathcal{L}(v_p)$ , to be a Gaussian, which are given by,

$$\mathcal{L}(v_r) \propto \exp\left(-\frac{1}{2}\left(\frac{v_r - \langle v_r \rangle}{\sigma_{v_r}}\right)^2\right), \quad \mathcal{L}(v_p) \propto \exp\left(-\frac{1}{2}\left(\frac{v_p - \langle v_p \rangle}{\sigma_{v_p}}\right)^2\right), \quad (11)$$

where  $\langle v_r \rangle = 3327\text{km s}^{-1}$ ,  $\sigma_{v_r} = 72\text{km s}^{-1}$ ,  $\langle v_p \rangle = 310\text{km s}^{-1}$  and  $\sigma_{v_p} = 150\text{km s}^{-1}$ .

As a result, the posterior  $p(H_0, D, v_p)$  is given by

$$\begin{aligned} p(H_0, D, v_p) &= \mathcal{L}(H_0, D, v_p) \pi(H_0, D, v_p) \times \frac{1}{\mathcal{N}_s(H_0)} \\ &\propto \exp\left(-\frac{1}{2}\left(\frac{v_p - \langle v_p \rangle}{\sigma_{v_p}}\right)^2\right) \times \exp\left(-\frac{1}{2}\left(\frac{H_0 D + v_p - \langle v_r \rangle}{\sigma_{v_r}}\right)^2\right) \\ &\times p(D) \times \pi(H_0) \times \pi(v_p) \times \frac{1}{\mathcal{N}_s(H_0)}, \end{aligned} \quad (12)$$

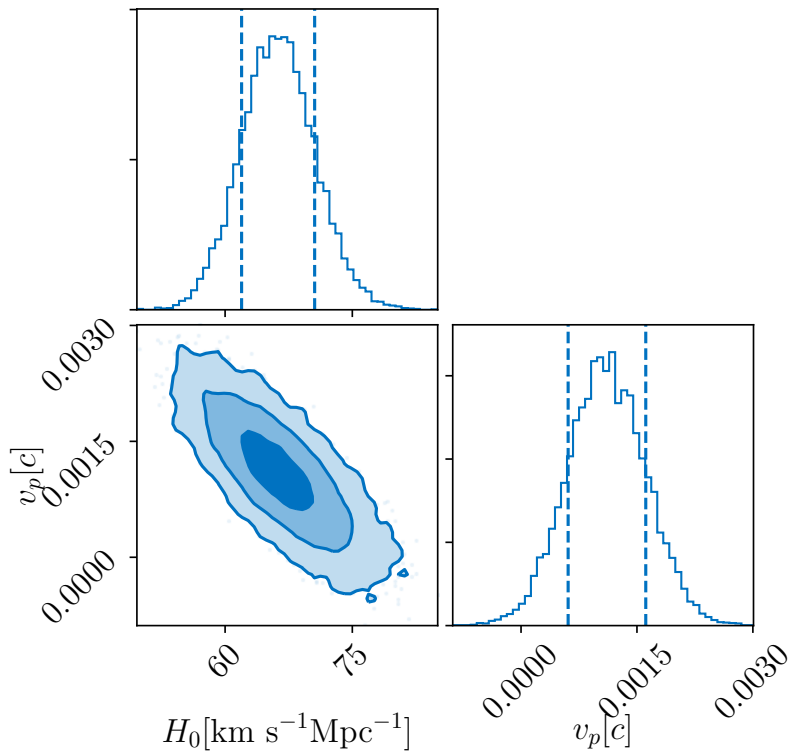


FIG. 13. Corner plot of the inferred  $H_0$ - $v_p$  with the posterior on the distance with combined analysis given.

where  $p(D)$ ,  $\pi(H_0)$  and  $\pi(v_p)$  are the posterior of the distance, the prior on the Hubble constant, and the prior on the peculiar velocity, respectively. And  $\mathcal{N}_s(H_0)$  is the selection effect term as described in [4]. We take  $\pi(H_0)$  to be uniform in  $[20, 160]\text{km s}^{-1}\text{Mpc}^{-1}$ ,  $\pi(v_p)$  to be uniform in  $[-c, c]$  and  $\mathcal{N}_s(H_0) \propto H_0^3$ . [109]

For the posterior of the distance, we take the posterior based on the combined analysis as described above. As we have a set of posterior samples  $\{d_i\}$  which follows the posterior  $p_{\text{com}}(D)$ , we obtain the marginalized posterior  $p(H_0, v_p)$  by

$$\begin{aligned}
 p(H_0, v_p) &= \int dD p(H_0, D, v_p) \\
 &= \int dD p_{\text{com}}(D) \frac{p(H_0, D, v_p)}{p_{\text{com}}(D)} \\
 &= \left\langle \frac{p(H_0, D, v_p)}{p_{\text{com}}(D)} \right\rangle_{\{d_i\}},
 \end{aligned} \tag{13}$$

in which we approximate  $\int dD p_{\text{com}}(D)$  by average over posterior sample  $\langle \dots \rangle_{\{d_i\}}$ . We sample over the  $p(H_0, v_p)$  with `emcee` [110] and obtain the corner plot shown in Fig. 13.